Carbon 253 (2026) 121429

Contents lists available at ScienceDirect

Carbon

journal homepage: www.elsevier.com/locate/carbon

Confinement-tuned magnetic competition and spin-asymmetric transport in quasi-one-dimensional $NiCl_2$ confined within carbon nanotubes

Waqas Saeed [a,*], Aleksandra Fidler [a], Piotr Dłużewski [a], Jeremy Sloan [b], Anna Kaleta [a], Martin R. Lees [b], Craig I. Hiley [c], Slawomir Kret [a]

[a] Institute of Physics, Polish Academy of Sciences, Aleja Lotników 32/46, 02-668, Warsaw, Poland
[b] Department of Physics, University of Warwick, Coventry, CV4 7AL, United Kingdom
[c] Department of Chemistry, University of Warwick, Coventry, CV4 7AL, United Kingdom

ARTICLE INFO

Keywords:
Carbon nanotubes
Confined metal halides
Low-dimensional magnetism
Spin-polarized electronic structure
Density functional theory
Spin-dependent transport

ABSTRACT

Encapsulation within single-walled carbon nanotubes (SWCNTs) provides a route to stabilize quasi-1D confined halide fragments derived from layered $NiCl_2$ and to tune their electronic and magnetic responses. Here we combine high-resolution STEM/EDS and spin-polarized DFT + U calculations to examine $NiCl_2$ fragments confined inside metallic (11,11) SWCNTs. Encapsulated $NiCl_2$ forms structurally continuous confined fragments derived from the layered $NiCl_2$ motif, consistent with the extended filling observed experimentally, in which the collinear FM configuration is energetically preferred (0 K) within the strongly confined (11,11) reference model, while larger diameters bring FM and AFM closer in energy (and can favor AFM), in contrast to antiferromagnetic bulk $NiCl_2$ (see SI). Spin-resolved PDOS and band analyses indicate that the pronounced Ni 3d spin-down peak at the Fermi level originates from weakly dispersive states, while CNT π-derived bands contribute the dominant delocalized channels at charge neutrality. Transport metrics suggest a confinement-related DOS–velocity mismatch that suppresses spin-down transport tendencies at neutrality while enabling increased spin-down contribution under modest chemical-potential shifts (≈+0.1–0.2 eV). Our results suggest that $NiCl_2$@SWCNT provides a case study for exploring how confinement tunes magnetic competition and spin-dependent transport tendencies in low-dimensional halide guests.

1. Introduction

Single-walled carbon nanotubes (SWCNTs) provide atomically smooth one-dimensional cavities that can host and often stabilize materials unstable in the corresponding bulk form. Their chemically inert interiors, well-defined diameters, and quasi-1D confinement make them ideal platforms for exploring structural, magnetic, and electronic phenomena that may not appear in extended crystals [1–3]. Confinement quantizes carrier dispersion, produces van Hove singularities, and enhances the sensitivity of transport to small shifts in chemical potential [4,5]. These effects, combined with tunable host–guest interactions, make CNT-based hybrid structures attractive for studying emergent magnetic and spin-dependent behavior.

Low-dimensional halides and related reduced-dimensional magnetic systems have attracted broad interest because confinement and reduced coordination can strongly modify magnetic ordering and electronic structure [6–12]. Separately, single-walled carbon nanotubes (SWCNTs) are well-established one-dimensional hosts for encapsulating ionic and halide-based guests, including one-dimensional crystals and halide/salt nanostructures, enabling confinement-stabilized structures and host–guest electronic effects [13–16,17–19,20,21]. However, despite growing interest in confined halide guests, the relationship between CNT confinement, magnetic ground-state stabilization, and spin-resolved conduction mechanisms remains largely unexplored.

While several studies have examined the encapsulation of metal halides and correlated chains inside SWCNTs [13–16,17–19,20,21], prior work has focused mainly on structural incorporation and average electronic shifts. In contrast, whether confinement can favor a collinear FM configuration (0 K) relative to AFM in $NiCl_2$ fragments, and the spin-resolved transport mechanisms that emerge from CNT–guest

* Corresponding author.
E-mail address: wsaeed@ifpan.edu.pl (W. Saeed).

https://doi.org/10.1016/j.carbon.2026.121429
Received 29 December 2025; Received in revised form 25 February 2026; Accepted 4 March 2026
Available online 11 March 2026

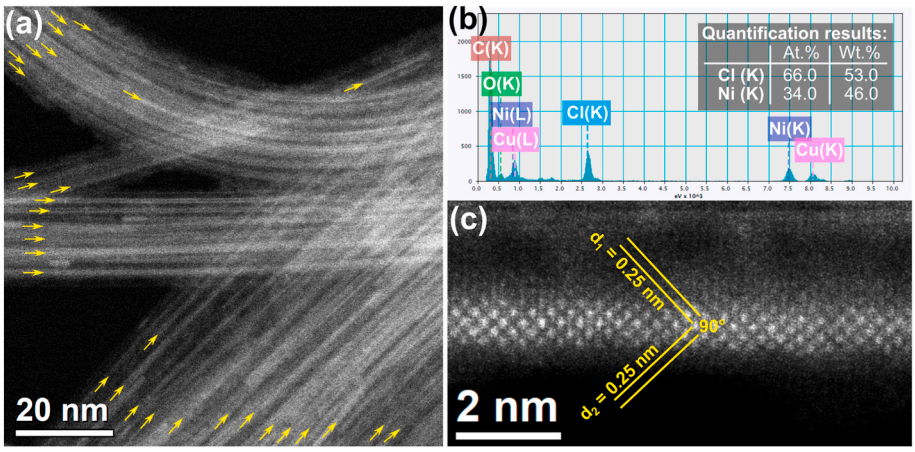

Fig. 1. (a) STEM-HAADF image of the SWCNTs after the filling procedure. Due to high Z-contrast of the $NiCl_2$ filling, a very high rate of filling can be observed. (b) EDS spectrum of the sample with the quantification results for $NiCl_2$ stoichiometry-confirmation. (c) STEM- HAADF image of a single encapsulated $NiCl_2$ nanocrystal with measured interplanar spacings and angle.

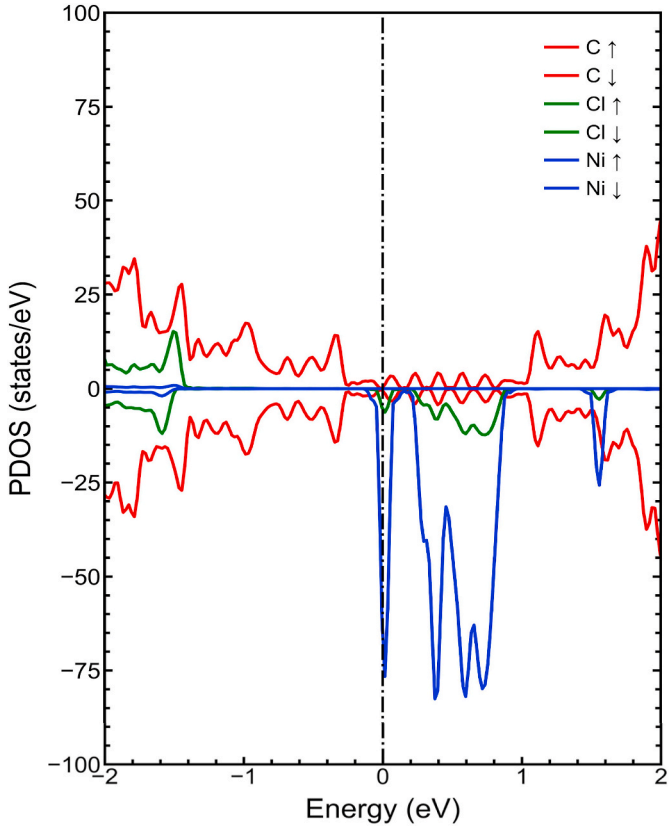

Fig. 2. Ab initio spin-resolved projected density of states (PDOS) for $NiCl_2$ confined inside a metallic (11,11) CNT. Red, green, and blue curves denote C, Cl, and Ni atoms, with positive and negative axes for spin-up and spin-down channels. A sharp Ni 3d spin-down peak at the Fermi level (E_F = 0 eV) reflects a pronounced quasi-1D van Hove–like feature associated with confinement-limited dispersion, establishing DOS-level spin asymmetry. (For interpretation of the references to colour in this figure legend, the reader is referred to the Web version of this article.)

hybridization, have not been addressed. Bulk $NiCl_2$ is an antiferromagnetic insulator [22,23], making the confinement-induced magnetic behavior particularly relevant.

More broadly, prior studies of confined halide guests in carbon nanotubes have emphasized structural incorporation, charge transfer, and average density-of-states modifications. The present work instead focuses on how confinement reshapes band dispersion, spatial localization, and spin-resolved velocity contributions, revealing a mismatch between DOS and transport tendencies that is not accessible from DOS analysis alone.

Here, we present the experimental realization of $NiCl_2$ in detail through STEM/EDS data extended with spin-polarized DFT + U theoretical calculations to show that $NiCl_2$ forms a **s**tructurally continuous, confinement-stabilized quasi-1D fragment derived from the layered $NiCl_2$ motif, consistent with the bilayer-limited configurations observed experimentally, inside metallic (11,11) SWCNTs with FM stabilization obtained for the (11,11) reference model; additional diameter/chirality checks indicate the system lies close to an FM/AFM crossover (see SI). Using COHP, Bader, velocity-weighted transport, BoltzTraP2 conductivity, and IPR analyses, we identify a confinement-induced DOS–velocity mismatch that suppresses transport from non-dispersive Ni spin-down states at neutrality. Modest chemical-potential shifts (≈+0.1–0.2 eV) bring more dispersive Ni spin-down bands into the relevant energy window, enhancing spin-asymmetric transport tendencies within the velocity-weighted/Boltzmann metrics.

Together, these results suggest $NiCl_2$@SWCNT as a case study system for studying confinement-stabilized magnetism and spin-dependent transport in confined halide fragments, and they further highlight the role of CNTs as active hosts that control electronic dispersion, localization, and spin asymmetry.

2. Experimental foundation

$NiCl_2$@SWCNT composites were first obtained experimentally via a melt filling approach, following established protocols [17–19,24,21]. Synthesis details are provided in the Supporting Information. In order to evaluate the results of the filling procedure, the samples of the obtained material were subjected to a scanning transmission electron microscopy (STEM) investigation with a use of FEI Titan Cubed 80-300 microscope. It was operated at 300 kV in STEM mode for high angle annular dark field (HAADF) imaging. The accelerating voltage was selected to ensure adequate contrast in this mode. Beam damage to the nanotubes, which can be significant at 300 kV, was prevented by lowering the electron beam current below 200 pA. No degradation of the encapsulated filling material was therefore observed during the imaging process. The elemental composition was determined by Energy Dispersive X-ray Spectroscopy (EDS) using EDAX 30 mm^2 Si (Li) detector, having a collection angle of 0.13 srad. Spectra were collected from the bundles of filled SWCNTs.

Low-magnification STEM imaging shows a high filling degree of the SWCNTs (i.e., >80–90%). For most SWCNTs, encapsulation extends

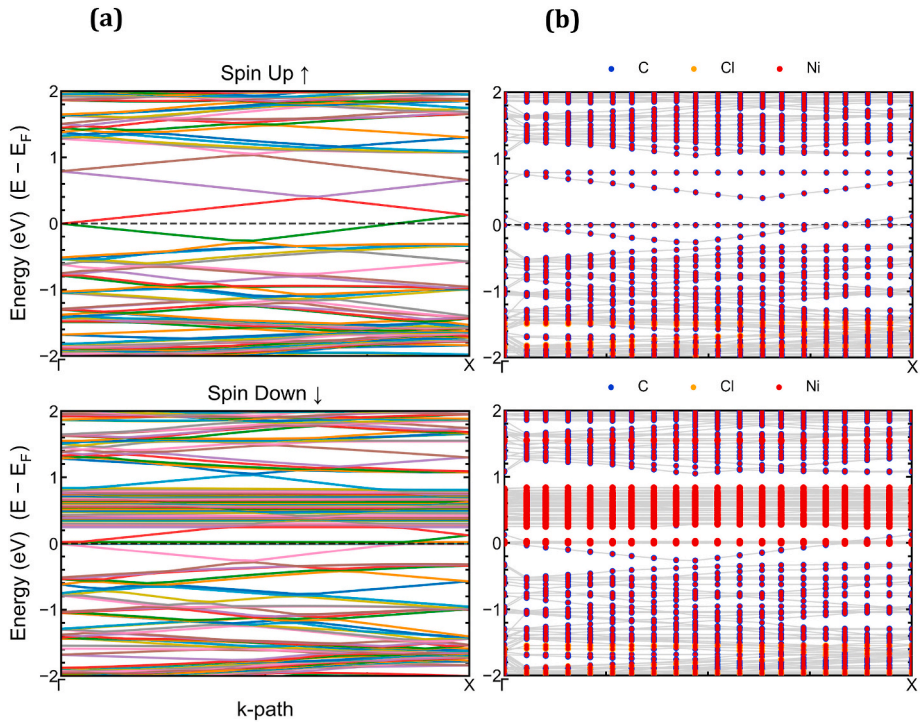

Fig. 3. (a) Spin-polarized electronic band structures of $NiCl_2$@SWCNT for spin-up (top) and spin-down (bottom) channels along Γ–X. The Fermi level is shown by the dashed line. Spin-up bands (CNT π/π*) are dispersive and cross E_F, while Ni 3d-derived spin-down bands are comparatively flat near E_F, giving rise to the asymmetric PDOS as seen in Fig. 2. (b) Element-projected fat-band structures for spin-up (top) and spin-down (bottom) channels. Marker sizes indicate contributions from C (blue), Cl (orange), and Ni (red). (For interpretation of the references to colour in this figure legend, the reader is referred to the Web version of this article.)

continuously over several hundred nanometers (Fig. 1a), which is clearly visualized in this imaging mode due to the high Z-contrast of the $NiCl_2$ filling. The transverse dimensions of the filled nanostructures depend on the nanotube diameter and range from approximately 1.5 to 2 nm. The elemental composition of the filled SWCNTs was verified by local EDS analysis of nanotube bundles, confirming the expected $NiCl_2$ stoichiometry of the encapsulated phase (Fig. 1b). Crystalline $NiCl_2$ adopts a $CdCl_2$-type layered structure with R-3mH symmetry (Fig. SI2a) [25]. STEM observations indicate that the confined structures correspond to fragments derived from this layered motif. Structural agreement was evaluated by comparing interatomic distances and angles measured from the experimental images with literature values for bulk $NiCl_2$ [25]. Due to confinement, in the STEM images examined here, no more than two $NiCl_2$ layers are observed inside individual nanotubes, appearing in different projections. In some cases, two distinct layers can be resolved, while in others the layers are rotated such that their projections overlap (Fig. 1c). Based on the latter configuration (Fig. SI2b), a preliminary structural model of $NiCl_2$ confined within a single-walled carbon nanotube was constructed (Fig. SI2c) and used as the starting point for structural relaxation and electronic-structure calculations. STEM image simulations based on the relaxed structure (Fig. SI4b) show good agreement with the experimental STEM image (Fig. 1c), supporting the structural consistency of the model. The observed confined motifs are also consistent with prior structural analysis of $NiCl_2$ encapsulated in SWCNTs [20,21], which similarly report bilayer-derived configurations. These observations indicate that the theoretical model used in this work represents a strongly confined bilayer-derived motif that is consistent with the structural motifs observed in the experimental STEM images. At the same time, some structural variability is expected across the sample depending on nanotube diameter and local filling conditions. The present model therefore serves as a representative confinement-limited reference structure for examining how strong confinement modifies magnetic competition relative to the bulk-like coordination limit.

To provide experimental context for the magnetic behavior, bulk SQUID magnetometry measurements were performed on the $NiCl_2$@SWCNT composites, and the key results are summarized in the main text, with full data provided in Supporting Information Section S2. The measurements show low-temperature magnetic irreversibility, finite but relatively small hysteresis, and a positive Curie–Weiss temperature. As an ensemble probe, SQUID magnetometry reflects the collective magnetic response of the composite and does not uniquely isolate individual confined fragments.

3. Methods

Density-functional theory calculations were performed on an initial structural model constructed from experimental STEM observations using spin-polarized PBE [26] and PAW potentials [27] as implemented in VASP [26,27], including dispersion via D3(BJ) [28] and a $U_{eff} = 4$ eV correction on Ni 3d states following prior work on $NiCl_2$ halides [29] within the Dudarev formulation [30]. Brillouin-zone sampling used a Monkhorst–Pack k-point grid [31]. A plane-wave cutoff of 450 eV and an (11,11) metallic SWCNT containing a commensurate $NiCl_2$ fragment (more details in Supporting Information, Section S3) were used; atomic positions were relaxed until forces were <0.01 eV $Å^{-1}$. Ferromagnetic (FM) and antiferromagnetic (AFM) configurations were initialized separately and relaxed independently; unless stated otherwise, reported energy differences compare these independently relaxed magnetic states. Additional FM–AFM energy comparisons for $NiCl_2$ fragments in (10,10), (11,11), (15,15), (17,0) and (18,0) SWCNTs were performed to check the variation of magnetic competition across different tube diameters, chiralities and U values; (17,0) and (18,0) were evaluated as fixed-geometry single-point checks (more details in SI table T1-T6). Electronic-structure analyses (PDOS, fat bands, charge-density differences, Bader charges) employed VASPKIT [32], pymatgen [33], and the Bader method [34,35]. Bonding interactions were evaluated using spin-resolved COHP [36] via LOBSTER [37]. Transport tendencies were

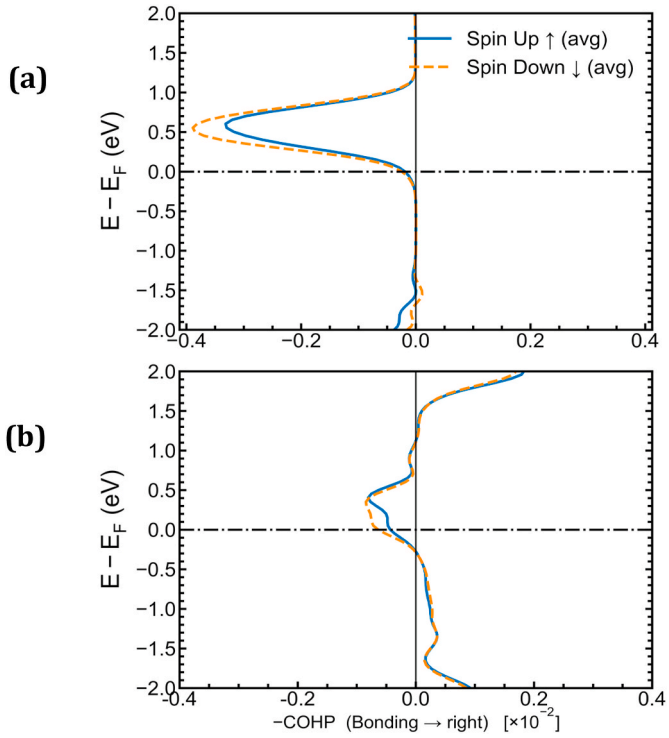

Fig. 4. (a) Spin-resolved COHP analysis for Ni–Cl interactions in $NiCl_2$@SWCNT. (b) Ni–C interactions in $NiCl_2$@SWCNT. COHP is plotted as −COHP, so positive values correspond to bonding contributions and negative values to antibonding contributions relative to E_F. For both (a) and (b), spin-up (solid) and spin-down (dashed) curves nearly overlap, indicating essentially spin-independent Ni–Cl and Ni–C bonding. The comparable bonding/antibonding distributions indicate that the observed spin asymmetry arises primarily from differences in band dispersion and localization rather than from bonding asymmetry.

assessed with velocity-weighted metrics derived from non-self-consistent band structures [38–42], while semiclassical conductivity was obtained using BoltzTraP2 [43,44]. BoltzTraP2 results are reported as σ/τ trends within the constant-relaxation-time approximation; absolute conductivities are not claimed because they require an explicit relaxation time τ. Localization and band dispersion were further analyzed using the inverse participation ratio (IPR) formalism [45,46].

Full computational parameters, transport theory, IPR formalism, and experimental procedures are provided in the Supporting Information.

4. Results — electronic structure

4.1. Spin-resolved projected density of states (PDOS)

The spin-resolved PDOS (Fig. 2) shows a pronounced Ni 3d spin-down peak at the Fermi level (E_F), characteristic of non-dispersive states in the confined $NiCl_2$ fragment. These narrow spin-down states dominate the DOS near E_F and give rise to a pronounced quasi-1D van Hove-like feature associated with confinement-limited dispersion. In contrast, the spin-up DOS at E_F is weak and largely CNT-derived, consistent with the metallic (11,11) host providing the available dispersive π and π^* channels at charge neutrality. Chlorine contributes only modest weight near E_F, reflecting its role in Ni–Cl bonding rather than conduction.

It is important to note that the PDOS alone does not convey band dispersion or transport activity: the large spin-down peak arises from localized Ni 3d states with low group velocity. As shown in the following sections, these Ni-dominated states are electronically significant but become transport-active only when dispersive hybridized bands enter the Fermi window under modest chemical-potential shifts. The PDOS therefore establishes the spin asymmetry in the electronic structure but does not by itself determine the active conduction channel.

4.2. Spin-resolved band structure

The spin-polarized band structures (Fig. 3a) reveal that both spin channels exhibit states intersecting E_F, but with distinct orbital origins. In the spin-up channel, the bands crossing E_F are primarily CNT π and π^* states with clear dispersion, consistent with their high group velocity and metallic character. In contrast, the spin-down channel contains several Ni-derived states near E_F, many of which are weakly dispersive and correspond to the localized 3d features identified in the PDOS.

Element-projected fat-band plots (Fig. 3b) confirm that the dispersive E_F crossings in the spin-up sector carry negligible Ni weight, while the spin-down states display significant Ni 3d character. This coexistence of dispersive CNT states and non-dispersive Ni states explains the strong spin asymmetry observed in the PDOS and establishes that, at charge neutrality, the CNT provides the dominant delocalized pathways, whereas the Ni spin-down states are electronically present but remain low-mobility.

4.3. COHP analysis

Spin-resolved COHP (Fig. 4a and b) indicates that bonding near E_F is dominated by Ni–Cl interactions, with only weak Ni–C contributions, and that the bonding framework is essentially spin-independent. The observed spin asymmetry is therefore better attributed to differences in band dispersion and localization than to spin-dependent bonding; details and sign conventions are provided in the Supporting Information (Section S5).

4.4. Charge redistribution, magnetic moments, and anisotropy

Charge-density difference maps (Fig. 5b) and Bader analysis (Table 1) show a consistent polar-covalent Ni–Cl bonding pattern, with charge depleted from Ni and accumulated on Cl. The CNT carbons

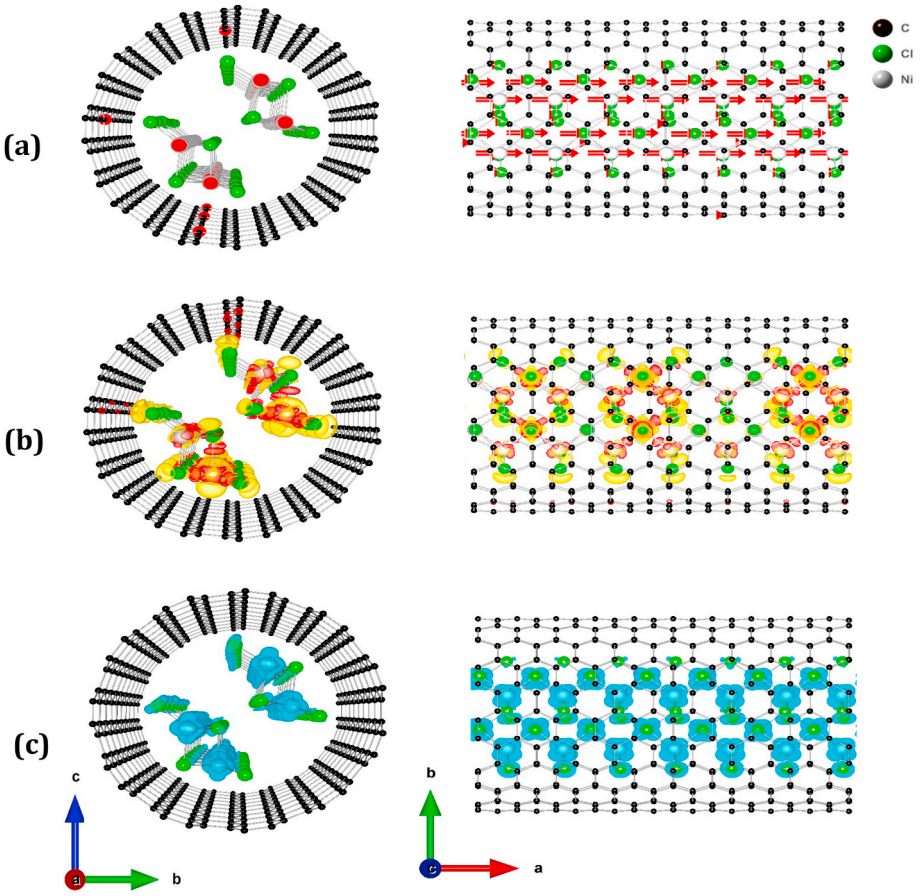

Fig. 5. (a) Ni magnetic-moment distribution along the quasi-1D fragment/chain. Red arrows indicate the direction of local Ni magnetic moments; arrow length is proportional to moment magnitude (μB). (b) Charge-density difference (Δρ = ρNiCl2@SWCNT − ρSWCNT − ρNiCl2) plotted at ±0.001 e Å^{-3}. Yellow and red isosurfaces represent charge accumulation and depletion, respectively. Electrons accumulate on Cl and deplete from Ni, consistent with polar-covalent Ni–Cl bonding, while the CNT shows only weak inner-wall polarization. (c) Spin-density isosurfaces (Δρspin = ρ↑ − ρ↓) for $NiCl_2$@SWCNT, plotted at ±0.008 e Å^{-3}. Cyan isosurfaces represent majority-spin density, which is localized on Ni 3d orbitals with minor polarization on Cl atoms. (For interpretation of the references to colour in this figure legend, the reader is referred to the Web version of this article.)

Table 1
A small residual charge imbalance (<0.1 e per formula unit) arises from grid discretization and does not affect the relative trends.

Species	N	Mean Charge (e)	Charge Transfer (lost/gain) (e)	Mean Moment (μB)
C	440	3.996	−0.003 (lost)	0.000
Cl	56	7.347	+0.347 (gain)	0.131
Ni	28	9.367	−0.633 (lost)	1.650

remain nearly neutral, confirming minimal host–guest charge transfer and supporting the interpretation that the CNT primarily acts as a weakly interacting confining host. Despite the charge redistribution, Ni atoms retain substantial local magnetic moments (~1.7 μB).

For the strongly confined reference model, total-energy comparisons indicate that a ferromagnetic alignment is energetically favored over the collinear antiferromagnetic configuration, in contrast to bulk $NiCl_2$ [22, 23]. However, across the tube-geometry sweep the FM–AFM energy differences are small and can change sign, indicating proximity to a confinement-controlled magnetic crossover. Accordingly, FM is favored for the more strongly confined (10,10)/(11,11) models, whereas the larger-diameter (15,15) tube favors AFM; zigzag (17,0)/(18,0) single-point checks retain an FM preference (SI, Tables T1–T6). Visualization of the spin density (Fig. 5c) illustrates the collinear FM spin polarization in the converged DFT + U solution along the confined fragment.

This magnetic competition is consistent with confinement-induced structural distortions that modify exchange pathways. The confined fragments retain the edge-sharing Ni–Cl–Ni geometry near ~90°, where antiferromagnetic superexchange is weakened and ferromagnetic contributions can become competitive, while more bulk-like coordination and angle evolution can strengthen antiferromagnetic tendencies (see Supporting Information, Section S3.3). Confinement-induced changes in bond angles, Ni–Ni separations, and local coordination therefore provide a structural basis for this confinement-controlled magnetic crossover. Experimentally, larger-diameter nanotubes may accommodate thicker fragments with more bulk-like coordination, consistent with the calculated trend toward AFM stabilization as confinement weakens.

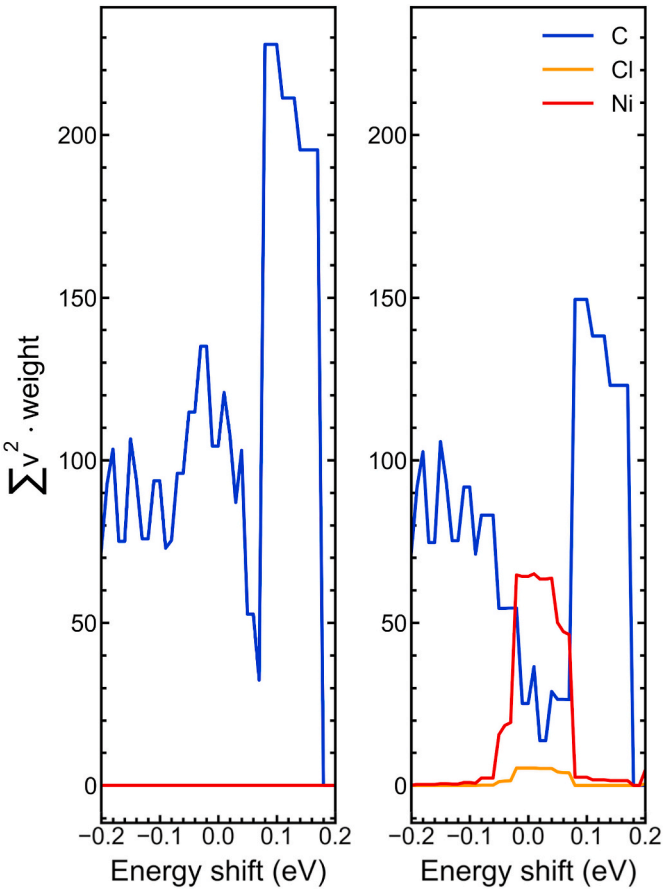

Fig. 6. Element-resolved velocity-weighted transport function ($\sum v^2$) versus Fermi-level shift for spin-up (left) and spin-down (right) channels. CNT (C) states dominate the spin-up transport tendency, while Ni 3d contributions emerge in the spin-down channel near E_F. The onset of Ni weight for small positive $\mu - E_F$ reflects entry of more dispersive Ni spin-down states into the transport window.

To address magnetic anisotropy, we estimated the magnetocrystalline anisotropy energy (MAE) by including spin–orbit coupling (SOC) for the relaxed reference structure at fixed geometry. The easy axis is parallel to the tube axis (1 0 0), and the MAE is on the order of ~1–2 meV per supercell (≈46–64 μeV per Ni); full details are provided in the Supporting Information. Our magnetic analysis is therefore limited to ground-state energetic competition between collinear FM and AFM configurations and the associated anisotropy, rather than a determination of finite-temperature magnetic ordering. Accordingly, we do not estimate an ordering temperature (e.g., TC) in this work. Possible non-collinear magnetic textures (e.g., canted or spiral states) are not explored here; SOC is included only for the purpose of evaluating the MAE.

Bulk SQUID magnetometry on $NiCl_2$@SWCNT composites shows a nontrivial low-temperature magnetic response (ZFC/FCC irreversibility and a positive Curie–Weiss θ; SI Section S2), consistent with net ferromagnetic exchange tendencies in the composite. Owing to its ensemble nature, this measurement does not uniquely assign the signal to the confined $NiCl_2$ fragments nor establish long-range ferromagnetic order, but it supports the presence of confinement-modified magnetic interactions relative to bulk $NiCl_2$.

4.5. Velocity-weighted transport analysis

The velocity-weighted transport function Gs(E) (Fig. 6) reveals that at charge neutrality, the spin-up channel dominates the transport tendency due to the strong dispersion of CNT π-derived states. In the spin-down channel, the Ni 3d states that create the pronounced DOS peak at E_F contribute little to G↓(E), reflecting their negligible group velocity.

As the chemical potential is shifted upward by +0.1–0.2 eV, moderately dispersive Ni spin-down bands enter the Fermi window, leading to a marked increase in G↓(E). This crossover is reflected in the spin-polarization P(E) (Fig. 7a), which evolves from weakly positive at charge neutrality to negative over the +0.1–0.2 eV range. The analysis indicates that confinement leads to a situation where CNT-derived dispersive states dominate the transport tendency at neutrality, while Ni-derived dispersive states become active only under modest chemical-potential shifts.

4.6. BoltzTraP2 conductivity along the tube axis

BoltzTraP2 calculations of conductivity per relaxation time (σ/τ) along the tube axis (Fig. 8) corroborate the velocity-weighted analysis. At $\mu - E_F = 0$, σ/τ is relatively low, consistent with the limited contribution of dispersive bands near E_F. As μ is shifted upward by +0.1–0.2 eV, σ/τ increases by roughly a factor of two, reflecting the entry of more dispersive Ni-derived states into the transport window. Although the calculation is spin-summed, the conductivity trend is consistent with the spin-resolved picture. This indicates that the confinement-stabilized hybrid exhibits a transport response governed primarily by the energetic alignment of dispersive bands rather than by the magnitude of the DOS alone.

Chemical-potential shifts of 0.1–0.2 eV are accessible in CNT electronic platforms via electrostatic gating, charge-transfer doping, and

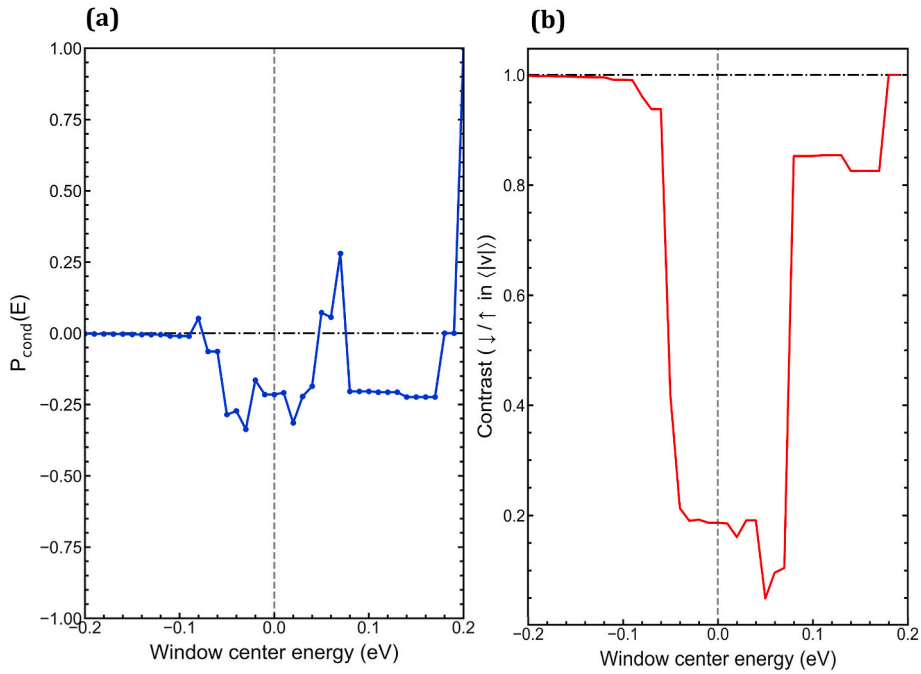

Fig. 7. (a) Calculated velocity-weighted transport spin polarization proxy P(E) versus Energy from the velocity-weighted model. P(E) remains near zero below E_F and becomes strongly negative for small positive $\mu - E_F$, indicating spin-down–dominant transport once dispersive Ni 3d states enter the conduction window. (b) Spin-velocity contrast ($|v\downarrow|/|v\uparrow|$) as a function of energy. A pronounced dip near E_F indicates reduced spin-down velocity at neutrality, while the ratio approaches unity away from E_F where both spins contribute comparably—capturing the μ-shift–driven transition from weak to strong spin-down conduction.

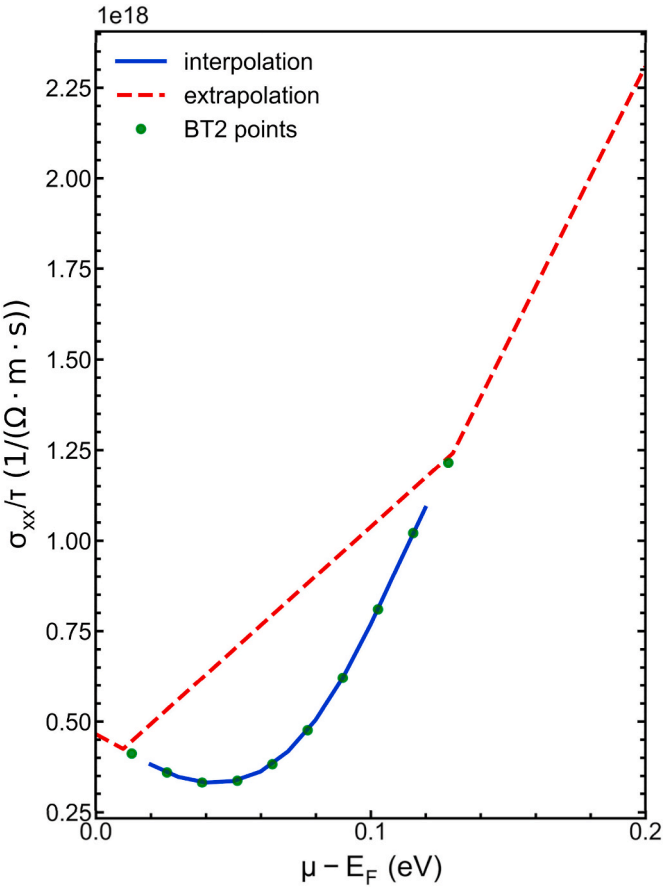

Fig. 8. BoltzTraP2-calculated conductivity per relaxation time, σ_{xx}/τ (in units of $10^{18}\ \Omega^{-1}\ m^{-1}\ s^{-1}$), as a function of chemical potential at 300 K. Interpolated (solid) and extrapolated (dashed) lines trace discrete BoltzTraP2 data (green). Conductivity increases sharply for small positive $\mu - E_F$, indicating entry of dispersive Ni 3d states above E_F, in agreement with the velocity-weighted analysis. (For interpretation of the references to colour in this figure legend, the reader is referred to the Web version of this article.)

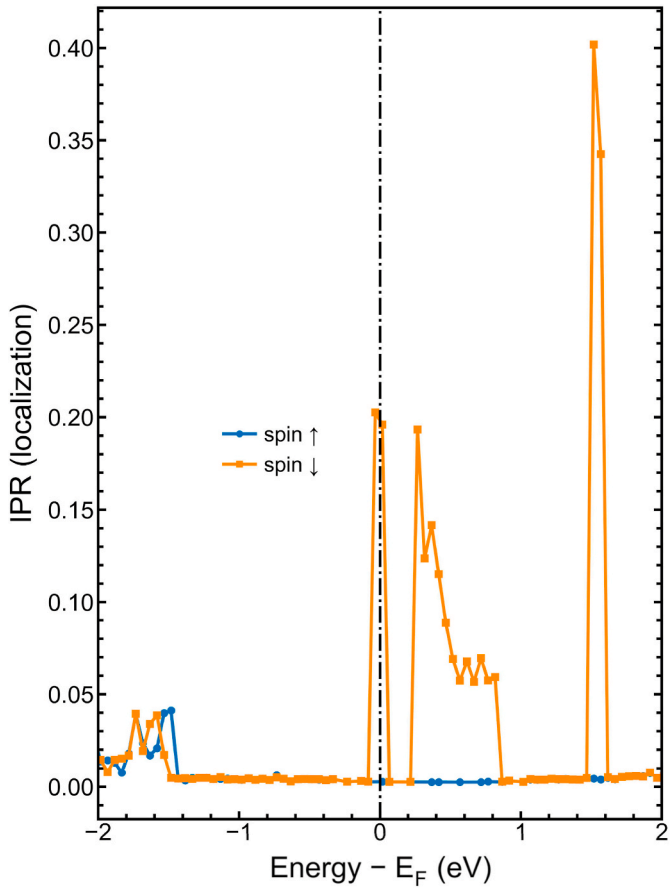

Fig. 9. Inverse participation ratio (IPR) versus energy for spin-up and spin-down states. Low IPR values for spin-up states indicate delocalized CNT-derived conduction. High IPR peaks for Ni spin-down bands near E_F reflect localization of non-dispersive 3d states, explaining their strong DOS but weak transport contribution.

contact effects [47–50]; here we treat this as a plausible tuning window for $NiCl_2$@SWCNT (via CNT-host gating/doping), rather than a demonstrated control in the present composite.

4.7. Inverse participation ratio (IPR) analysis

The IPR spectra (Figs. 9 and 10) distinguish localized and delocalized states and directly support the transport interpretation. In the spin-up channel, states crossing E_F show low IPR values, confirming their delocalized, CNT-derived character. In the spin-down channel, the Ni 3d states at E_F exhibit high IPR values, indicating spatial localization and explaining their limited transport contribution despite their large DOS.

With increasing energy (+0.1–0.2 eV), spin-down states become more delocalized, consistent with the dispersive bands responsible for the conductivity increase identified in Fig. 8. At higher energies, the IPR rises again, reflecting the reappearance of localized Ni-derived states. These results show that the interplay of confinement-stabilized localization and CNT-enabled dispersion underlies the observed spin-dependent transport behavior.

5. Conclusion

Encapsulation of $NiCl_2$ inside metallic SWCNTs yields a structurally stable confined fragment derived from the layered $NiCl_2$ motif, in which magnetic competition is modified by confinement. In the strongly confined reference model, the collinear ferromagnetic configuration is energetically preferred, whereas increasing the tube diameter drives the system toward (or into) an AFM regime (see SI). This behavior contrasts with bulk $NiCl_2$, which is antiferromagnetic, and is consistent with confinement-modified magnetic competition reported in other low-dimensional halide and nanotube-based systems. Spin-resolved electronic-structure analysis shows that the prominent Ni 3d spin-down DOS at the Fermi level arises from weakly dispersive, low-velocity states, while dispersive CNT π bands provide the dominant delocalized channels at charge neutrality. COHP and Bader analyses further indicate that the CNT acts as a weakly interacting yet structurally enabling host, largely preserving the intrinsic Ni–Cl bonding environment.

Transport metrics derived from velocity-weighted spectral functions and BoltzTraP2 calculations suggest that modest upward chemical-potential shifts increase the contribution of more dispersive Ni spin-down bands to transport. Localization trends from IPR calculations further support this crossover from localized to more delocalized Ni-derived states. Together, these results suggest a confinement-related link between electronic dispersion, spatial localization, and spin-dependent transport. $NiCl_2$@SWCNT therefore provides an experimentally grounded case study for exploring spin-asymmetric transport tendencies governed by the energetic alignment of dispersive bands in confinement-stabilized halide–CNT heterostructures. Future work could examine the influence of nanotube chirality and external gating, and assess whether related behavior extends to other transition-metal halide fragments. Comparable confinement-driven magnetic competition may occur in other divalent halides (e.g., $CoCl_2$ and $FeCl_2$), although the relative importance of the underlying exchange pathways is likely to depend on the d-electron configuration and the local coordination geometry.

CRediT authorship contribution statement

Waqas Saeed: Writing – review & editing, Writing – original draft, Methodology, Investigation, Formal analysis, Data curation,

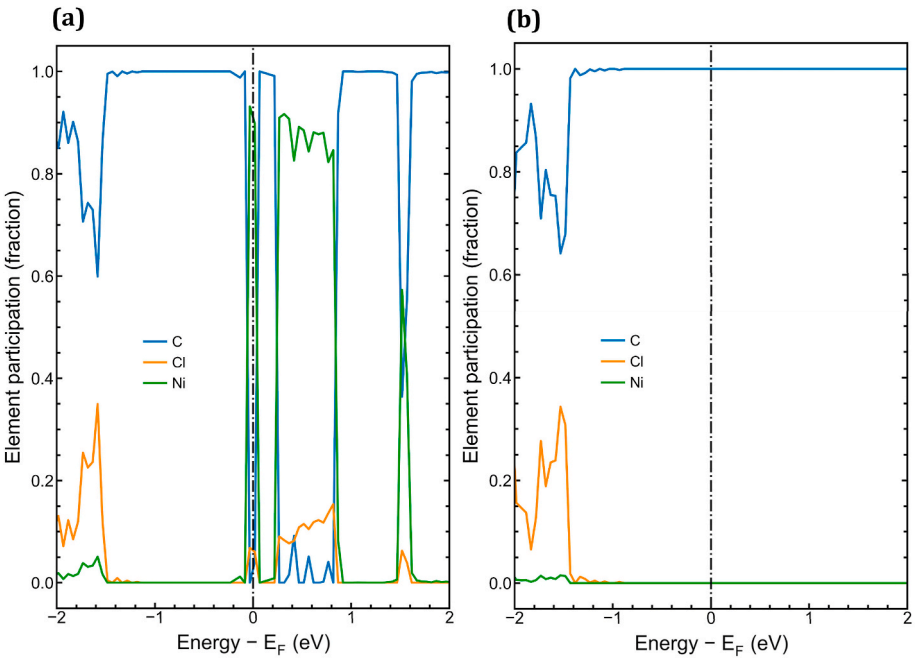

Fig. 10. (a) Elemental participation fractions versus energy for the spin-down channel. Contributions from C (blue), Cl (orange), and Ni (green) show that Ni 3d character dominates near E_F, while C (CNT) weight increases away from E_F. This redistribution marks the entry of dispersive Ni spin-down states into the transport window. (b) Element participation fractions versus energy for the spin-up channel. Conduction is dominated by CNT π and π* states, with negligible Ni contribution near E_F, illustrating the delocalized metallic character of the spin-up channel. (For interpretation of the references to colour in this figure legend, the reader is referred to the Web version of this article.)

Conceptualization. **Aleksandra Fidler:** Writing – original draft, Formal analysis, Data curation. **Piotr Dłużewski:** Writing – review & editing, Validation, Supervision, Methodology, Investigation. **Jeremy Sloan:** Writing – review & editing, Validation, Supervision, Methodology. **Anna Kaleta:** Visualization, Investigation. **Martin R. Lees:** Data curation. **Craig I. Hiley:** Data curation. **Slawomir Kret:** Supervision, Resources, Project administration, Funding acquisition, Formal analysis, Data curation.

Declaration of competing interest

The authors declare that they have no known competing financial interests or personal relationships that could have appeared to influence the work reported in this paper.

Acknowledgements

This work was supported by the National Science Centre (Poland) under Project No. UMO-2021/41/B/ST5/02588. Computational calculations were performed using resources provided by the Wrocław Centre for Networking and Supercomputing (WCSS) under computational grant hpc-waqas1-1749742312. The authors would like to thank Jakub Turczyński for technical assistance related to the experimental setup as well as Paweł Skupiński for sealing the reaction ampoules.

Appendix A. Supplementary data

Supplementary data to this article can be found online at https://doi.org/10.1016/j.carbon.2026.121429.

References

[1] S. Iijima, Helical microtubules of graphitic carbon, Nature 354 (1991) 56–58, https://doi.org/10.1038/354056a0.
[2] A. Jorio, G. Dresselhaus, M.S. Dresselhaus (Eds.), Carbon Nanotubes: Advanced Topics in the Synthesis, Structure, Properties and Applications, Springer, Berlin, 2008, https://doi.org/10.1007/978-3-540-72865-8.
[3] M. Monthioux, Filling single-wall carbon nanotubes, Carbon 40 (2002) 1809–1823, https://doi.org/10.1016/S0008-6223(02)00102-1.
[4] J.W. Mintmire, B.I. Dunlap, C.T. White, Are fullerene tubules metallic? Phys. Rev. Lett. 68 (1992) 631–634, https://doi.org/10.1103/PhysRevLett.68.631.
[5] T.W. Odom, J.-L. Huang, P. Kim, et al., Atomic structure and electronic properties of single-walled carbon nanotubes, Nature 391 (1998) 62–64, https://doi.org/10.1038/34145.
[6] T. Li, S. Jiang, N. Sivadas, et al., Pressure-controlled interlayer magnetism in atomically thin CrI_3, Nat. Mater. 18 (2019) 1303–1308, https://doi.org/10.1038/s41563-019-0506-1.
[7] S.P.M. Curley, R. Scatena, R.C. Williams, et al., Magnetic ground state of the one-dimensional ferromagnetic chain compounds $M(NCS)_2$(thiourea)$_2$ (M = Ni, Co), Phys. Rev. Mater. 5 (2021) 034401, https://doi.org/10.1103/PhysRevMaterials.5.034401.
[8] C. Gong, L. Li, Z. Li, et al., Discovery of intrinsic ferromagnetism in two-dimensional van der Waals crystals, Nature 546 (2017) 265–269, https://doi.org/10.1038/nature22060.
[9] B. Huang, G. Clark, E. Navarro-Moratalla, et al., Layer-dependent ferromagnetism in a van der Waals crystal down to the monolayer limit, Nature 546 (2017) 270–273, https://doi.org/10.1038/nature22391.
[10] I. Žutić, J. Fabian, S. Das Sarma, Spintronics: fundamentals and applications, Rev. Mod. Phys. 76 (2004) 323–410, https://doi.org/10.1103/RevModPhys.76.323.
[11] S.A. Wolf, D.D. Awschalom, R.A. Buhrman, et al., Spintronics: a spin-based electronics vision for the future, Science 294 (2001) 1488–1495, https://doi.org/10.1126/science.1065389.
[12] R. Waser, D.E. Bürgler, C.M. Schneider, M. Morgenstern, S. Blügel (Eds.), *Spintronics — from GMR to Quantum Information*, Lecture Notes of the 40th Spring School, Forschungszentrum Jülich GmbH Zentralbibliothek, Jülich, 2009. ISBN: 978-3-89336-559-3.
[13] A. Eliseev, L.V. Yashina, M.V. Kharlamova, et al., One-dimensional crystals inside single-walled carbon nanotubes: growth, structure and electronic properties, in: J. M. Marulanda (Ed.), Electronic Properties of Carbon Nanotubes, InTech, Rijeka, 2011, pp. 127–156, https://doi.org/10.5772/19060.
[14] G.M. Milligan, Z.-F. Yao, D.L. Mesoza Cordova, et al., Single quasi-onedimensional chains of Sb2Se3 encapsulated within single-walled carbon nanotubes, Chem. Mater. 36 (2024) 730–741, https://doi.org/10.1021/acs.chemmater.3c02114.
[15] Y. Lee, U. Choi, K. Kim, et al., Recent progress in realizing novel one-dimensional polymorphs via nanotube encapsulation, Nano Converg. 11 (2024) 52, https://doi.org/10.1186/s40580-024-00460-3.
[16] M.C. Giménez-López, F. Moro, A. La Torre, et al., Encapsulation of single-molecule magnets in carbon nanotubes, Nat. Commun. 2 (2011) 407, https://doi.org/10.1038/ncomms1415.
[17] P.M. Ajayan, S. Iijima, Capillarity-induced filling of carbon nanotubes, Nature 361 (1993) 333–334, https://doi.org/10.1038/361333a0.
[18] G. Brown, S.R. Bailey, M. Novotny, et al., High yield incorporation and washing properties of halides incorporated into single walled carbon nanotubes, Appl. Phys. A 76 (2003) 457–462, https://doi.org/10.1007/s00339-002-2040-1.

[19] C. Nie, A.-M. Galibert, B. Soula, et al., The unexpected complexity of filling double-wall carbon nanotubes with nickel (and iodine) 1D nanocrystals, IEEE Trans. Nanotechnol. 16 (2017) 759–767, https://doi.org/10.1109/TNANO.2017.2686434.
[20] K. Bal, Crystallography and Characterisation of Atomically Thin Confined Nanowires, University of Warwick, Coventry, UK, 2023. PhD thesis.
[21] M.V. Kharlamova, L.V. Yashina, A.A. Eliseev, et al., Single-walled carbon nanotubes filled with nickel halogenides: atomic structure and doping effect, Phys. Status Solidi B 249 (2012) 2328–2332, https://doi.org/10.1002/pssb.201200060.
[22] J.B. Goodenough, Magnetism and the Chemical Bond, Interscience, New York, 1963.
[23] M.E. Lines, Magnetic properties of $CoCl_2$, $NiCl_2$ and $FeCl_2$, Phys. Rev. 131 (1963) 546–555, https://doi.org/10.1103/PhysRev.131.546.
[24] O.A. Gurova, V.E. Arhipov, V.O. Koroteev, et al., Purification of single-walled carbon nanotubes using acid treatment and magnetic separation, Phys. Status Solidi B 256 (2019) 1800742, https://doi.org/10.1002/pssb.201800742.
[25] A. Ferrari, A. Braibanti, G. Bigliardi, Refinement of the crystal structure of $NiCl_2$ and of unit-cell parameters of some anhydrous chlorides of divalent metals, Acta Crystallogr. 16 (1963) 846–847, https://doi.org/10.1107/S0365110X63002231.
[26] G. Kresse, J. Furthmüller, Efficient iterative schemes for ab initio total-energy calculations using a plane-wave basis set, Phys. Rev. B 54 (1996) 11169–11186, https://doi.org/10.1103/PhysRevB.54.11169.
[27] G. Kresse, D. Joubert, From ultrasoft pseudopotentials to the projector augmented-wave method, Phys. Rev. B 59 (1999) 1758–1775, https://doi.org/10.1103/PhysRevB.59.1758.
[28] S. Grimme, J. Antony, S. Ehrlich, H. Krieg, A consistent and accurate ab initio parametrization of density functional dispersion correction (DFT-D) for the 94 elements H–Pu, J. Chem. Phys. 132 (2010) 154104, https://doi.org/10.1063/1.3382344.
[29] J.Y. Ni, X.Y. Li, D. Amoroso, X. He, J.S. Feng, E.J. Kan, S. Picozzi, H.J. Xiang, Giant biquadratic exchange in 2D magnets and its role in stabilizing ferromagnetism of $NiCl_2$ monolayers, Phys. Rev. Lett. 127 (2021) 247204, https://doi.org/10.1103/PhysRevLett.127.247204.
[30] S.L. Dudarev, G.A. Botton, S.Y. Savrasov, et al., Electron-energy-loss spectra and the structural stability of nickel oxide: an LSDA+U study, Phys. Rev. B 57 (1998) 1505–1509, https://doi.org/10.1103/PhysRevB.57.1505.
[31] H.J. Monkhorst, J.D. Pack, Special points for Brillouin-zone integrations, Phys. Rev. B 13 (1976) 5188–5192, https://doi.org/10.1103/PhysRevB.13.5188.
[32] V. Wang, N. Xu, J.-C. Liu, et al., VASPKIT: a user-friendly interface facilitating high-throughput computing and analysis using VASP code, Comput. Phys. Commun. 267 (2021) 108033, https://doi.org/10.1016/j.cpc.2021.108033.
[33] S.P. Ong, W.D. Richards, A. Jain, et al., Python materials genomics (pymatgen): a robust, open-source python library for materials analysis, Comput. Mater. Sci. 68 (2013) 314–319, https://doi.org/10.1016/j.commatsci.2012.10.028.
[34] G. Henkelman, A. Arnaldsson, H. Jónsson, A fast and robust algorithm for Bader decomposition of charge density, Comput. Mater. Sci. 36 (2006) 354–360, https://doi.org/10.1016/j.commatsci.2005.04.010.
[35] R.F.W. Bader, Atoms in Molecules: a Quantum Theory, Oxford University Press, Oxford, 1990.
[36] R. Dronskowski, P.E. Blöchl, Crystal orbital Hamilton populations (COHP): energy-resolved visualization of chemical bonding in solids based on density-functional calculations, J. Phys. Chem. 97 (1993) 8617–8624, https://doi.org/10.1021/j100135a014.
[37] R. Nelson, C. Ertural, J. George, et al., LOBSTER: local orbital projections, atomic charges, and chemical bonding analysis from projector-augmented-wave-based density-functional theory, J. Comput. Chem. 41 (2020) 1931–1940, https://doi.org/10.1002/jcc.26353.
[38] N.W. Ashcroft, N.D. Mermin, Solid State Physics, Saunders, Philadelphia, 1976.
[39] J.M. Ziman, Principles of the Theory of Solids, second ed., Cambridge University Press, Cambridge, 1972.
[40] M.P. Marder, Condensed Matter Physics, second ed., Wiley, New York, 2010.
[41] R. Kubo, Statistical-mechanical theory of irreversible processes. I. General theory and simple applications to magnetic and conduction problems, J. Phys. Soc. Jpn. 12 (1957) 570–586, https://doi.org/10.1143/JPSJ.12.570.
[42] D.A. Greenwood, The Boltzmann equation in the theory of electrical conduction in metals, Proc. Phys. Soc. 71 (1958) 585–596, https://doi.org/10.1088/0370-1328/71/4/306.
[43] G.K.H. Madsen, D.J. Singh, BoltzTraP. A code for calculating band-structure dependent quantities, Comput. Phys. Commun. 175 (2006) 67–71, https://doi.org/10.1016/j.cpc.2006.03.007.
[44] G.K.H. Madsen, J. Carrete, M.J. Verstraete, BoltzTraP2, a program for interpolating band structures and calculating semi-classical transport coefficients, Comput. Phys. Commun. 231 (2018) 140–145, https://doi.org/10.1016/j.cpc.2018.05.010.
[45] F. Wegner, Inverse participation ratio in $2+\varepsilon$ dimensions, Z. Phys. B 36 (1980) 209–214, https://doi.org/10.1007/BF01325284.
[46] R.J. Bell, P. Dean, Atomic vibrations in vitreous silica, Discuss. Faraday Soc. 50 (1970) 55–61, https://doi.org/10.1039/DF9705000055.
[47] K.K. Kim, J.J. Bae, H.K. Park, et al., Fermi level engineering of single-walled carbon nanotubes by $AuCl_3$ doping, J. Am. Chem. Soc. 130 (2008) 12757–12761, https://doi.org/10.1021/ja8038689.
[48] M. Krüger, M.R. Buitelaar, T. Nussbaumer, et al., Electrochemical carbon nanotube field-effect transistor, Appl. Phys. Lett. 78 (2001) 1291–1293, https://doi.org/10.1063/1.1350427.
[49] C. Klinke, J. Chen, A. Afzali, et al., Charge transfer induced polarity switching in carbon nanotube field-effect transistors, Nano Lett. 5 (2005) 555–558, https://doi.org/10.1021/nl048055c.
[50] W. Zhou, J. Vavro, N.M. Nemes, et al., Charge transfer and Fermi level shift in doped single-walled carbon nanotubes, Phys. Rev. B 71 (2005) 205423, https://doi.org/10.1103/PhysRevB.71.205423.